ACS APPLIED ENERGY MATERIALS

Open Access

This article is licensed under CC-BY 4.0

www.acsaem.org

Article

Polymorphic Effects and Optoelectronic Excellence in Mixed-Pb/Sn Halide Perovskites for Next-Generation Solar Harvesting

Danilo Neves Silveira,* Luis Octavio de Araujo, Marco Antônio Andrade Queiroz, Celso R. C. Rêgo, Carlos Maciel de O. Bastos, Maurício J. Piotrowski, Alexandre C. Dias, Fernando P. Sabino, and Diego Guedes-Sobrinho*

Cite This: *ACS Appl. Energy Mater.* 2026, 9, 9445−9455

Read Online

ACCESS | Metrics & More | Article Recommendations | Supporting Information

ABSTRACT: Polymorphic effects in mixed-metal halide perovskites (MHP) are critical for predicting optoelectronic performance, as the high-symmetry cubic phase ($Pm\bar{3}m$) alone is insufficient to explain observed performance. Here, we performed first-principles calculations with an advanced statistical model to describe the thermodynamic ensembles of $CsPb_{1-x}Sn_xCl_3$ and $CsPb_{1-x}Sn_xBr_3$, from which the optoelectronic behavior is described through polymorphic contributions by integrating an innovative workflow automation within the SimStack framework. We employed a generalized quasichemical approximation (GQCA) approach to perform a weighted contribution of different polymorphic degrees based on symmetry breaking to confer a more realistic description for the alloys, predominantly driven by distortions and rotations of the octahedra (e.g., based on Glazer's notations). We found that power conversion efficiencies at operating temperature for both materials exhibit maximum performance for $x > 0.70$, highlighting the value of ∼29% for the Br-based alloy, which present advantageous low critical temperatures of approximately 28 K (whereas it is 110 K for $CsPb_{1-x}Sn_xCl_3$). Therefore, mixing Sn and Pb as MHP alloys preserves high PCE values and mitigates the oxidation tendency of Sn-based MHPs in air, supporting the development of long-term stable photovoltaic devices.

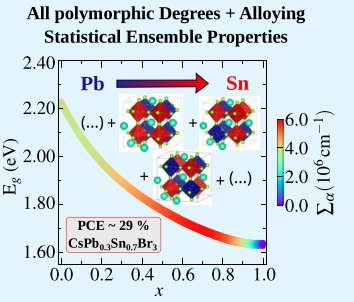

KEYWORDS: *metal halide perovskites, all-inorganic perovskite alloys, generalized quasichemical approximation, density functional theory, DFT-1/2, polymorphic degrees*

1. INTRODUCTION

The development of metal halide perovskites (MHPs) for photovoltaic applications has led to a significant focus on enhancing their stability without compromising efficiency, a primary research challenge in the field.[1,2] The hybrid MHPs have been the focus of attention for their high power conversion efficiencies (PCE), which have been shown to exceed 26% for $FAPbI_3$ single-junction solar cells (SCs),[3] comparable to other photovoltaic technologies, such as crystalline silicon and GaAs.[4,5] However, stability issues related to organic cations in MHPs – attributable to their hygroscopic and volatile characteristics – remain a critical obstacle in the development of long-lasting SCs, whereas all-inorganic MHPs implies an additional complexity due to the impact of the structural polymorphism.[6−10] Therefore, an important question emerges: how to perform a modeling in which relativistic contributions for the electronic description and polymorphic degree in mesoscale are simultaneously included to predict thermodynamic stability and PCE from a more realistic approach?

Mixture of metals in all-inorganic Cs-based MHPs has been proposed to the detriment of the single metal compositions, in particular, based on mitigating the quantities of toxic Pb[11] in the material manufacturing at the same time allowing easy control of their physical-chemical properties.[2,9] Sn-based alloys are promising candidates due to the similar atomic radius and oxidation states of Sn and Pb, which favor stable compound formation.[12] In this context, Sn-based compounds, such as $CsSnX_3$, exhibit smaller band gaps than their Pb counterparts, promoting a redshift in optical absorption and improving photovoltaic efficiency. However, understanding the impact of the mixed-Sn/Pb on the photovoltaic performance and thermodynamic stability at atomic scale based on polymorphic contributions is not trivial, being of central relevance in material design for photovoltaic applications.

For instance, the polymorphic nature of inorganic MHPs (e.g., metal off-center displacements within the octahedra, second-order Jahn-Teller distortions and their octahedra rotations, or positional disorder of cations at cavity sites) manifests at the local structural level, which is not always captured by

Received: April 29, 2026
Revised: June 15, 2026
Accepted: June 19, 2026
Published: July 8, 2026

Downloaded from http://pubs.acs.org/aaemcq/article-pdf/doi/10.1021/acsaem.6c01421/65829129/ae-2026-014215.pdf by KIT BIBLIOTHEK user on 27 July 2026

conventional X-ray diffraction techniques, given that they inherently probe average crystal structures over long coherence lengths.[13,14] Although advanced scattering methods (e.g., diffuse scattering, EXAFS) can provide local structural information,[15,16] resolving coexisting polymorphic states in alloys remains particularly challenging, especially as both the halide and metal compositions are varied simultaneously. Consequently, it is imperative to incorporate this behavior through appropriate theoretical protocols, weighing the contribution of each relevant polymorphic pattern to construct a physically meaningful description of the system.[9,17,18]

In this study, the thermodynamic and optoelectronic properties of $CsPb_{1-x}Sn_xX_3$ alloys (X = Cl, Br) are examined through building up a statistical ensemble of the alloys based on different contributions of polymorphic patterns. We have developed a workflow implementation within the SimStack framework to perform first principle calculations based on the density functional theory (DFT),[9,19−21] enabling efficient and systematic streamlining of high-throughput computational data processing. We built up the concept of all-polymorphic degrees (APD) as a generalized ensemble, which was able to provide precise descriptions of the properties of a given polymorphic patterns. Here, we have demonstrated that employing Cl and Br as halides in the composition implies the possibility of more distorted octahedrons.

2. COMPUTATIONAL AND THEORETICAL METHODS

2.1. Automation Method through the SimStack Framework

In order to investigate the average properties of $CsPb_{1-x}Sn_xCl_3$ and $CsPb_{1-x}Sn_xBr_3$ polymorphic structures, alloys ensemble configurations were created through supercell expansion of the $Pm\bar{3}m$ cubic structure. Through this expansion, as illustrated in Figure 1a, eight corresponding exchange sites were created to form the clusters expanding the alloys. The structured input is processed through an automated computational workflow implemented within the SimStack Framework,[21] which is summarized through its interface, as represented in Figure 1b, systematically coordinating the entire calculation pipeline. The raw data generation processes use the Workflow Active Nodes (WaNos), which standardize the sequence of computational steps and manage complex tasks like high-performance computing (HPC) connectivity and data retrieval. Additionally, a Colab notebook facilitates the extraction of average properties across the MHP alloys ensemble. This implementation is available on GitHub (https://github.com/KIT-Workflows/TMD-Alloy).

Below, we describe and show our automated workflow designed to determine average thermodynamic and optoelectronic properties for a statistical ensemble of polymorphic $CsPb_{1-x}Sn_xX_3$ (X = Cl and Br) alloys:

(1) **SOD-2022**: the SOD WaNo generates non-equivalent configurations through symmetry operations on the corresponding structure.[22] These configurations – known as clusters – form the alloy's statistical ensemble and are used to calculate its thermodynamic and optoelectronic properties as a function of composition. This protocol has been successfully used in several MHPs studies, demonstrating that each cluster remains statistically and energetically independent regarding the others.[9,23] Here, we construct the clusters through a 2 × 2 × 2 supercell, forming eight octahedral sites (Figure 1a) and systematically replacing Pb with Sn, resulting in $2^8 = 256$ configurations. Using SOD, we obtained 22 classes (J, with g_j as the degeneracy factor from which the 256 configurations are reduced) of the $CsPb_{1-x}Sn_xX_3$ alloys.

In these configurations, A designates the Pb sites and B the exchange for Sn metal through the sequence 12345678, thereby identifying the sites as AAAAAAAA, BAAAAAAA, ABBAAAAA, etc. As an example of an exchange, Figure 1c shows $n_j = 4$, which has six non-equivalent positions with their respective classes (j) and degeneracy factors (g_j) configurations that are used for the representation of the statistical ensemble. Non-equivalent structures, as well as their respective degeneracy factors, are shown in Figure S1 of the Supplementary Materials. Given the broad representativeness of the sample, the statistical significance of the sampling is evident in the context of treatment with the GQCA method.

(2) **Mult-It:** this WaNo promotes data generation and compilation within the workflow.[21] It results in lists of floating-point and integer numbers, concurrently with the reading of lists of filenames from *.tar files. Thus, data preparation is seamlessly passed to UnpackMol WaNo within the ForEach loop control, further improving workflow efficiency.

(3) **UnpackMol:** unpack SOD-2022 configuration files, making them available for further processing by DFT-VASP WaNo. It is fully integrated into the SimStack framework and runs within the ForEach loop control to efficiently process multiple configurations. This data preparation automation provides a smooth, optimized path from SOD-2022 output to DFT-VASP WaNo input, playing a key role in our workflow by streamlining data preparation for DFT calculations.

(4) **DFT-VASP:** it is a computational tool that facilitates the total energy and structural optimization of the $CsPb_{1-x}Sn_xCl_3$ and $CsPb_{1-x}Sn_xBr_3$ in ab initio computational calculations relied on the density functional theory (DFT) [24,25] approach, using the Perdew-Burke-Ernzerhof (PBE) [26] exchange–correlation (XC) functional. To solve the Kohn-Sham equations, we employed the projector-augmented plane wave (PAW) [27] method, implemented in the Vienna Ab initio Simulation Package (VASP),[28,29] in which fully relativistic calculations describe the core states. Furthermore, the valence states were treated with spin-orbit coupling (SOC) using a scalar-relativistic approximation.

The plane waves used within the PAW method were expanded up to a cutoff energy of 430 eV, considering the explicit configurations of the valence electrons: Cs ($5s^2$, $5p^6$, $6s^1$), Pb ($5s^2$, $5d^{10}$, $6s^2$, $6p^2$), Sn ($4d^{10}$, $5s^2$, $5p^2$), Cl ($3s^2$, $3p^5$), and Br ($4s^2$, $4p^5$). The Brillouin zone integration was performed considering a k–mesh of 4 × 4 × 4 Γ-centered grid of **k** points. The lattice constants, stress tensors, and ions positions were thoroughly optimized. The criterion for convergence of total energy in all polymorphic structures was defined as 1.0×10^{-5} eV and the Hellmann-Feynman forces were relaxed until their values were less than 0.010 eV $Å^{-1}$ in each atom.

(4.1) **Gap energies from DFT-1/2 quasiparticle correction:** The gap energies (E_g) were computed by employing the DFT-1/2 correction.[30,31] This correction is inspired by Slater's half-occupation technique,[30,32] being grounded in Janak's theorem,[33] which demonstrates that the orbital's energy eigenvalue with half-occupation equals the electron's ionization potential. This is accounted for through a modified KS potential ($V_{mod,KS}(\mathbf{r})$), which is obtained by subtracting the self-energy potential ($V_S(\mathbf{r})$) from the standard KS potential ($V_{KS}(\mathbf{r})$),

Downloaded from http://pubs.acs.org/aaemcq/article-pdf/doi/10.1021/acsaem.6c01421/65829129/ae-2026-014215.pdf by KIT BIBLIOTHEK user on 27 July 2026

https://doi.org/10.1021/acsaem.6c01421
ACS Appl. Energy Mater. 2026, 9, 9445−9455

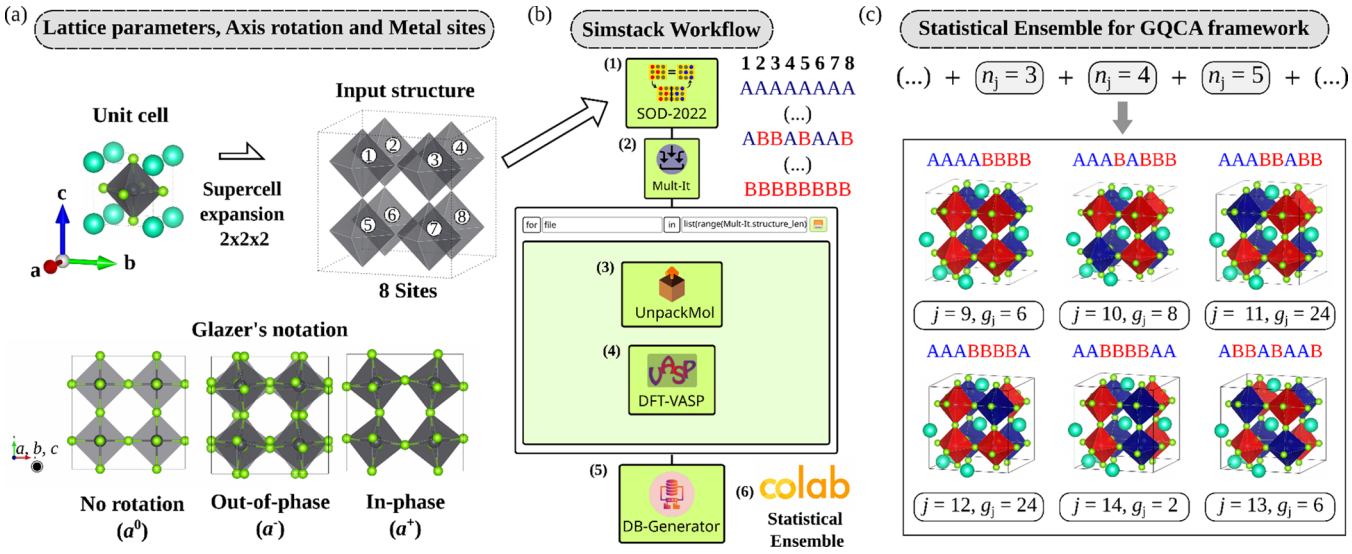

Figure 1. Representation of (a) super cell expansion of a cubic unit cell to form the cluster configurations expanding the $CsPb_{1-x}Sn_xX_3$ alloys and schematic representation of the Glazer's notation, in which superscripts 0, −, and + indicate, respectively, no rotation, out-of-phase, and in-phase rotation around the m (= a, b or c) axis along the viewing direction; (b) the SimStack framework that integrating several WaNos: (1) SOD-2022, (2) Mult-It, (3) UnpackMol, (4) DFT-VASP, (5) DB-generator, and (6) GQCA via Colab notebook; and (c) example of the substitution of 4 Pb → Sn of 6 classes (j) and its degeneracy factor (g_j). Octahedra in blue contain Pb at the center site, while the red octahedra contain Sn. In these classes, Pb is represented by A and Sn by B, according to the 12345678 sequence of site occupations.

i.e., $V_{mod,KS}(\mathbf{r}) = V_{KS}(\mathbf{r}) - V_S(\mathbf{r})$. In such expression, $V_S(\mathbf{r})$ is acquired from the KS potentials associated with neutral ($V_0(\mathbf{r})$) and half-ionized atoms ($V_{-1/2}(\mathbf{r})$), with ionization performed from the 3p and 4p orbitals of pure compositions of Cl and Br, respectively, applied in different polymorphic configurations. Therefore, $V_S(\mathbf{r}) = \Theta(\mathbf{r}, \mathrm{CUT})[V_0(\mathbf{r}) - V_{-1/2}(\mathbf{r})]$, where $\Theta(\mathbf{r}, \mathrm{CUT})$ is a step function introduced to prevent the potential interpenetration between neighbor atoms, whose optimal value of CUT parameter is determined through the maximization of the E_g values without experimental parameters. For the purposes of this study, CUT values of 3.1 a_0 were employed for $CsPb_{1-x}Sn_xCl_3$, and 3.3 a_0 for $CsPb_{1-x}Sn_xBr_3$. Details about this variational procedure for $CsPbCl_3$, $CsPbBr_3$, $CsSnCl_3$ and $CsSnBr_3$ MHPs can be accessed in the Figure S2 in Supplementary Materials.

(4.2) **PCE from the spectroscopy limited maximum efficiency (SLME) model**: To evaluate the photovoltaic efficiency of $CsPb_{1-x}Sn_xX_3$ alloys as a function of composition, the Spectroscopic Limited Maximum Efficiency (SLME) model was employed.[34] To simulate *in operando* conditions, the material thickness was fixed at l = 1 μm and the temperature at T = 300 K. The SLME approach offers a more comprehensive framework than the standard Shockley-Queisser (SQ) model,[35] as it explicitly incorporates the material's finite thickness (l) and its energy-dependent optical absorption coefficient ($\alpha(\omega)$).

For the calculation of the optical absorption coefficient ($\alpha_j(\omega)$), each expanded j of the represented polymorphs of the $CsPb_{1-x}Sn_xX_3$ alloys was considered, using the gap corrected by DFT-1/2 with SOC. It was used the expression [36,37]

$$\alpha_j(\omega) = \frac{\sqrt{2}\omega}{c}\left[\sqrt{\epsilon^2_{\mathrm{Re},j}(\omega) + \epsilon^2_{\mathrm{Im},j}(\omega)} - \epsilon_{\mathrm{Re},j}(\omega)\right]^{1/2}$$

with ω being the photon energy, c represents the speed of light in vacuum, $\epsilon_{\mathrm{Re},j}(\omega)$ is the real part, and $\epsilon_{\mathrm{Im},j}(\omega)$ the imaginary part of the dielectric function. $\epsilon_{\mathrm{Im},j}(\omega)$ was computed within the random phase approximation (RPA),[38] whereas $\epsilon_{\mathrm{Re},j}(\omega)$ was obtained through the Kramers–Kronig transformation.[39] The alloys' absorption coefficients were then evaluated as the GQCA ensemble average, i.e., $\alpha(\omega;x, T) = \sum_j x_j(x, T)\,\alpha_j(\omega)$,[40,41] where the cluster absorption coefficient was derived from the x, y, and z components of the dielectric tensor.[42]

(5) **DB-Generator:** automates the generation of YAML files with degeneracy factors and total energies from ab initio calculations. These files feed directly into a Colab notebook, enabling the construction of alloy phase diagrams and the evaluation of their thermodynamic properties.

(6) **GQCA via Colab notebook:** the statistical ensembles of the $CsPb_{1-x}Sn_xX_3$ (X = Cl or Br) alloys were constructed based on the GQCA formalism. By considering the $CsBX_3$ (B = Sn, Pb, and X = Cl or Br) MHPs as polymorphous networks, distortions from the ideal $Pm\bar{3}m$ structure were allowed to occur in the alloys. This primarily included B metal off-center displacements within octahedra,[18] positional rearrangements of Cs ions within the cuboctahedral cavities,[43] and octahedra rotations.[44] The latter was denoted through the Glazer's notation.[45] In this notation, strings are associated with the magnitude (a, b or c), and superscripts with the relative orientation (a^0 for no rotation, a^+ for in-phase rotation, and a^- for out-of-phase rotation) of the octahedral tilts along each crystallographic axis. When the rotation magnitudes differ between axes, a new letter is introduced to distinguish these degrees of freedom. For example, in $a^0b^-b^+$, the letter b indicates a rotation magnitude on the b and c axes different from that on a. This notation is schematized in Figure 1a and detailed in Figure S3 in Supplementary Materials.

To assess the impact of Glazer's patterns on the structural and electronic properties of the alloys investigated here, we initially selected five Glazer's patterns to configure the clusters expanding the alloy: $a^0a^0a^0$ (monomorphic $Pm\bar{3}m$ structure),

https://doi.org/10.1021/acsaem.6c01421
ACS Appl. Energy Mater. 2026, 9, 9445−9455

Downloaded from http://pubs.acs.org/aaemcq/article-pdf/doi/10.1021/acsaem.6c01421/65829129/ae-2026-014215.pdf by KIT BIBLIOTHEK user on 27 July 2026

$a^0b^+b^+$, $a^0b^-b^+$, $a^+a^-a^+$ and $a^-a^+a^-$. This selection was based on our previous studies regarding MHPs as polymorphous networks. As shown in previous work by our group,[8,10,46,47] polymorphic structures are energetically more stable than the unrotated cubic pattern $a^0a^0a^0$, and the APD ensemble was constructed to encompass both lower energy configurations, $a^0b^+b^+$ and $a^0b^-b^+$, and structurally distinct alternating patterns, $a^+a^-a^+$ and $a^-a^+a^-$, ensuring a more representative sampling of the material's phase space. To consider the possibility of all these polymorphs in the alloys simultaneously, we constructed a generalized ensemble containing clusters from all structures (110 per halide's composition) termed the all polymorphic degrees (APD) ensemble. Thus, APD ensemble is constructed by considering $a^0a^0a^0$ + $a^0b^+b^+$ + $a^0b^-b^+$ + $a^+a^-a^+$ + $a^-a^+a^-$. This generalized ensemble approach was previously used to describe heterostructural alloys[48] and also $CsPb_{1-x}Sn_xI_3$,[46] being used here to expand $CsPb_{1-x}Sn_xX_3$ into the cubic structure, considering various possibilities of structural motifs that may be present in their polymorphic networks.[8,13]

From the g_j obtained by the SOD-2022 Wanos, associated with the equivalent structures, and excess energy:

$$\Delta\varepsilon_j = E_j - \frac{n-n_j}{n}E_{CsPbX_3} - \frac{n_j}{n}E_{CsSnX_3} \quad (1)$$

with $\Delta\varepsilon_j$ being named the excess energy of the j-th class, the occurrence probability x_j was estimated by minimizing the Helmholtz free energy: $\Delta_{mix}F(x, T) = \Delta_{mix}U(x, T) - T\Delta_{mix}S(x, T)$, where the internal energy is given $\Delta_{mix}U(x, T) = \sum_{j=1}^{J} x_j(x, T)\Delta\varepsilon_j$ and the entropy term is derived from the Kullback–Leibler (KL) divergence between the alloy's probability distribution and that of a regular solid solution. With respect to the APD dataset, these energies represent the excess energy of each configuration relative to the most stable structures, as determined by the convex hull approach.[49−52] The KL divergence and details of all the equations and their definitions are available and discussed in Figure S4 of Supplementary Materials.

3. RESULTS

3.1. Structural Properties and Thermodynamic Behavior of Alloys

The calculated lattice parameters for the $CsPb_{1-x}Sn_xCl_3$ and $CsPb_{1-x}Sn_xBr_3$ alloys demonstrate a excellent agreement with experimental findings, exhibiting a maximum deviation of approximately 2%.[53,54] These parameters follow Vegard's law closely[55] within the $a^0a^0a^0$ polymorph, characterized by a linear decrease driven by the reduced radius of Sn compared to Pb. Deviations in lower-symmetry polymorphs are attributed to structural distortions, resulting in anisotropy (particularly in $a^0b^+b^+$ and $a^0b^-b^+$) and subtle alterations in b and c. In this region, the bond lengths of the B–X type exhibit a comparable variation in accordance with composition. The numerical values, as well as the graphical representation of the variation of a, b, and c with composition, are presented in Figure S5 and Tables S2–S11 in the Supplementary Materials.

In order to observe the impact of composition and polymorphs on the local structure, the B–Cl (B–Br) distances and B–Cl–B (B–Br–B) angles were characterized for the alloys in all Glazer's configurations, whose results are shown in Figure 2, their numerical values are presented in Tables S12–S21 in the Supplementary material. The distinct atomic radii of Pb and Sn occupying the B sites of the BX_6^{2-} sublattice introduce a size mismatch that tends to increase lattice distortions upon Sn incorporation. By comparing the data from $CsPb_{1-x}Sn_xCl_3$ (panels a–e) and $CsPb_{1-x}Sn_xBr_3$ (panels k–o), the polymorphic patterns exhibit a similar behavior in the B–X bond lengths regardless of the halide species. The panels (b) and (c) ((l) and (m)) show the greater intervals covered by the highest and the lowest B–X distances for configuration at both 0 and 300 K. Notably, the polymorph $a^0b^+b^+$ exhibits a stronger tendency towards metal decentralization (metal off-centering profile), driven by the stereochemically active lone pair of Sn.[56] This tendency towards metal off-centering is identified as a stabilizing mechanism for these compounds, as pointed out in previous studies.[8] As the out-of-phase polymorph, $a^0b^-b^+$ (c and m) and $a^+a^-a^+$ (e and t), is analyzed, it is possible to observe the suppressive effect of the off-center metal on B site. The out-of-phase rotations effectively counteract the distortions introduced by Sn incorporation and leading to a more regular coordination environment. The effect, confirmed by the observations of structural motifs, tends to be similar to those of the $a^0a^0a^0$ polymorph in panels (a, k). Furthermore, the larger atomic radius of Pb relative to Sn expands the effective cavity size within the lattice,[10] while the polymorphic diversity provides an improved coordination site with reduced lattice strain.

With regard to the bond angles, a contrasting trend is observed in the presence of Cl or Br in the solid solution. For the $CsPb_{1-x}Sn_xCl_3$ alloys, the alternation of the in-phase/no-rotation ↔ out-of-phase ↔ in-phase configurations shows an abrupt decline in symmetry as the Sn metal is incorporated into the lattice, as evidenced in panels (h) and (j). Among the configurations examined, those exhibiting in-phase rotations, particularly $a^+a^-a^+$, display the lowest overall lattice symmetry, consistent with the reduced point-group symmetry expected for such tilt patterns. The observed behavior can be attributed to the Cl atom's radius relative to the metallic sites. The incorporation of small halides into the crystal lattice increases the sensitivity of the octahedral rotations, generating a symmetry break in the angles and deviating from the symmetry patterns of the polymorphic structures. These results are not observed in Br alloys, as well as in I alloys,[46] which reinforces the role of atomic radii in governing the structural response of the lattice to compositional changes.

To evaluate the energetic favorability of alloying in the $CsPb_{1-x}Sn_xCl_3$ and $CsPb_{1-x}Sn_xBr_3$ systems, we quantified the internal energy of mixing, $\Delta_{mix}U(x, T)$, employing an APD statistical ensemble. As illustrated in Figure 3, the mixing energy data reveal the excess energy of each configuration relative to the ground-state pure compounds. The discrete energetic contributions of individual clusters are represented by open symbols, providing a granular view of the configurational landscape and the competing interactions governing the stability of the solid solution.

At $T = 0$ K, most j configurations exhibited positive excess energies, with the mixtures between $CsSnX_3$ and $CsPbX_3$ reaching the lowest excess energies in the polymorphic alloys, especially for the $a^+a^-a^+$ and $a^-a^+a^-$ configurations, which represent the low symmetry patterns and exhibit greater stability due to the better cavity/Cs compatibility. However, those positive values do not mean that the mixing is unfavorable;

https://doi.org/10.1021/acsaem.6c01421
ACS Appl. Energy Mater. 2026, 9, 9445−9455

Downloaded from http://pubs.acs.org/aaemcq/article-pdf/doi/10.1021/acsaem.6c01421/65829129/ae-2026-014215.pdf by KIT BIBLIOTHEK user on 27 July 2026

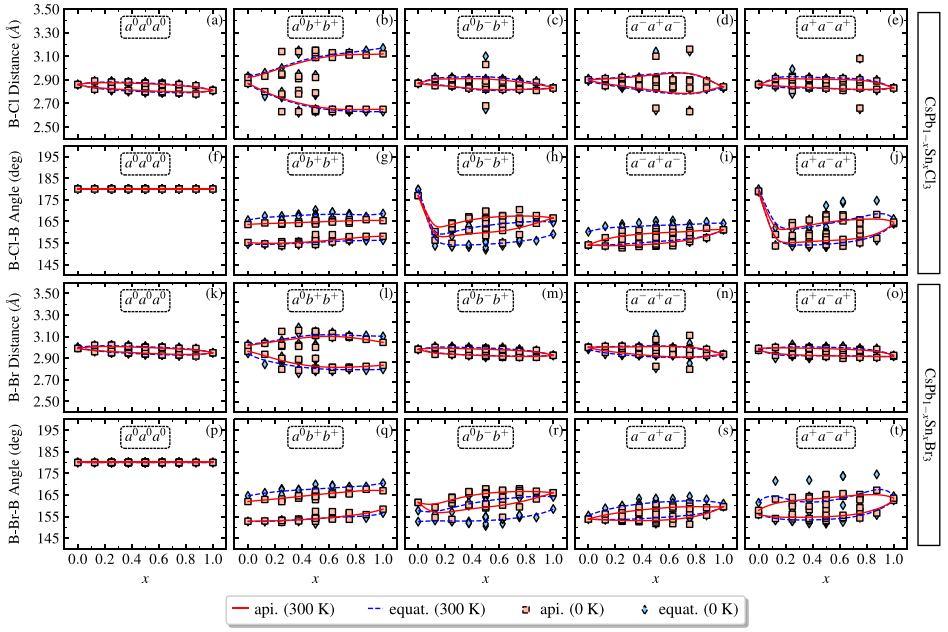

Figure 2. Structural parameters calculated for clusters (scatter) and their average at 300 K calculated as a function of composition (x) for $CsPb_{1-x}Sn_xCl_3$ (a, f) $a^0a^0a^0$, (b, g) $a^0b^-b^+$, (c, h) $a^0b^+b^+$, (d, i) $a^+a^-a^+$, and (e, j) $a^-a^+a^-$ polymorph alloys and $CsPb_{1-x}Sn_xBr_3$ (k, p) $a^0a^0a^0$, (l, q) $a^0b^-b^+$, (m, r) $a^0b^+b^+$, (n, s) $a^+a^-a^+$, and (o, t) $a^-a^+a^-$ polymorph alloys.

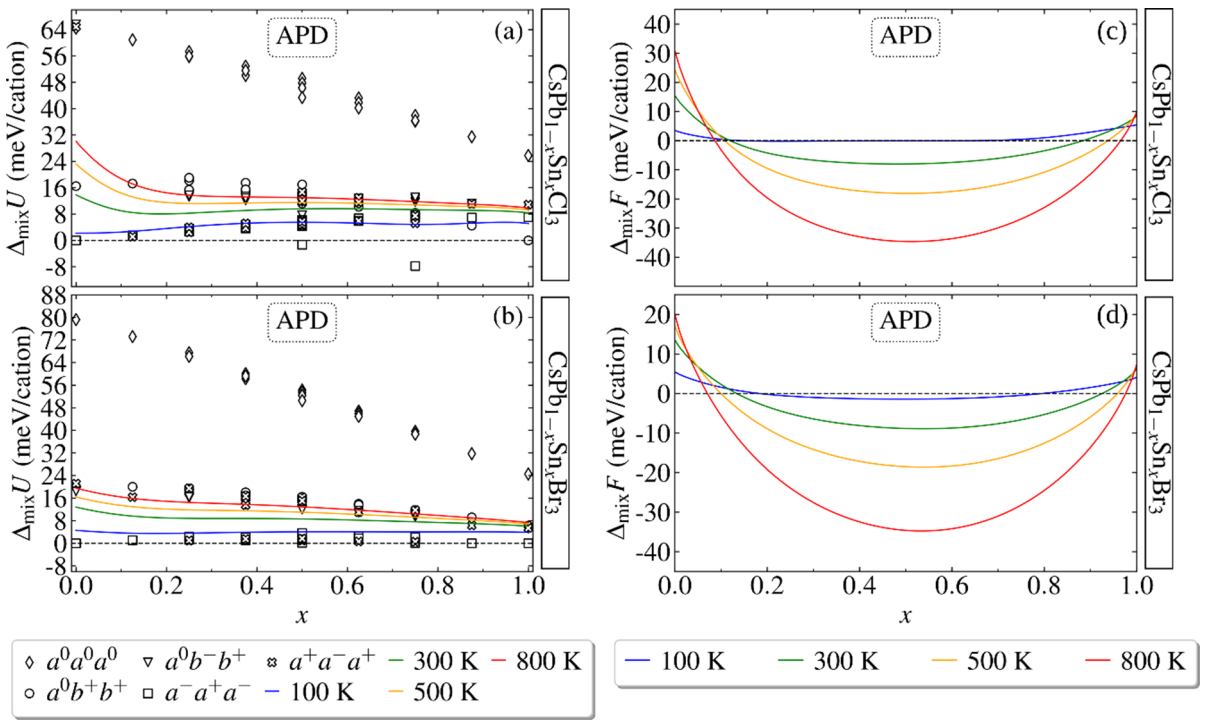

Figure 3. Excess energy (scatter) and mixing internal energies ($\Delta_{mix}U$) vs composition (x) at 100–800 K, considering all polymorphic degrees (APD), for (a) $CsPb_{1-x}Sn_xCl_3$ and (b) $CsPb_{1-x}Sn_xBr_3$. Mixing free energies ($\Delta_{mix}F$) vs x in the same temperature range for (c) and (d), respectively.

rather, they indicate that all configurational contributions (through entropy) must be considered to verify the energy favorability of the alloy formation. Noteworthy, at the alloy's isostructural limit, denoted as $a^0a^0a^0$, substantial $\Delta\varepsilon_j$ values were observed, exhibiting a tendency to decrease with increasing Sn composition for high values of x. The trend differs from other contributions involving more distorted polymorphic structures, indicating that the high-symmetry polymorphic pattern is less unstable in the presence of the Pb. Furthermore, we present the dependence of $\Delta_{mix}U(x, T)$ on temperature.

Downloaded from http://pubs.acs.org/aaemcq/article-pdf/doi/10.1021/acsaem.6c01421/65829129/ae-2026-014215.pdf by KIT BIBLIOTHEK user on 27 July 2026

https://doi.org/10.1021/acsaem.6c01421
ACS Appl. Energy Mater. 2026, 9, 9445−9455

To explain the observed behavior, Figure 4 shows the probabilities x_k as a function of the composition of all polymorphic contributions. At cryogenic temperatures (30 to 100 K), the predominant contribution of the polymorphic pattern is $a^-a^+a^-$ for the pure compositions, both for $CsPb_{1-x}Sn_xCl_3$ and $CsPb_{1-x}Sn_xBr_3$. Since these represent the most stable polymorphs, their dominant contributions to x_k lower the free energy curves as a function of temperature, thereby enhancing the thermodynamic stability of the alloys. Moreover, a convergence of other polymorphic structures, with contributions from x_k, is observed as the temperature increases.

Considering the possibility of miscibility gaps for MHP alloys at room temperature, the stability regarding the free energy of mixing ($\Delta_{mix}F$) as a function of temperature was also analyzed, as shown for the APD configuration in Figure 3. In addition to the energetic contribution described above, configurational entropy effects are presented by each isostructural polymorph in Figure S6 of the Supplementary Materials. The results demonstrate the instability of the alloys at the limits of pure Pb and Sn compositions, as a consequence of positive excess energy of $\Delta_{mix}U$. Using the convex hull formalism, $\Delta_{mix}F$ profiles in Figure 3 show a favorable mixing of $CsPbX_3$ and $CsSnX_3$ in the temperature range 100 K $< T <$ 800 K since all curves are below the straight line connecting these compounds in their metastable structures at $T > 0$ K. In addition, the results indicate a subtle trend towards greater stability in alloys with excess Sn. Along with the greater instability of alloys near the $CsPbCl_3$ limit, this demonstrates how the compatibility of the halide's atomic size with the metal is essential, especially for the less symmetrical polymorphic patterns and the greater stability resulting from octahedral distortions. As indicated in the structural analyses related to the metal off-centering in polymorphic patterns, the compatibility between the components is contingent on the capacity to coordinate Cs with the halides and to accommodate the cation without generating stress in the crystal lattice. This supports the lower stability of Cl-based systems in comparison to Br-based ones.

In order to verify how polymorphic contributions affect the stability and metastability of $CsPb_{1-x}Sn_xX_3$ against phase segregation as a function of composition and temperature, we computed their T-x phase diagrams from the respective free energy profiles. The results are shown in Figure 5a for $CsPb_{1-x}Sn_xCl_3$, and $CsPb_{1-x}Sn_xBr_3$ in (b), and the isostructural Glazer's polymorphs results can be found in the Figure S7 in Supplementary Materials.

We found two critical temperatures for $CsPb_{1-x}Sn_xCl_3$ alloy, located at $0.25 < x < 0.61$ and $0.95 < x < 0.98$ at $T = 116.6$ K and $T = 102.8$ K, respectively. In $CsPb_{1-x}Sn_xBr_3$, a miscibility gap between 0.05 and 0.67 is observed, with a critical temperature of 28.3 K, considerably lower than that of the chlorine-based alloy. As demonstrated in Figure 3 and indicated at critical temperatures, the $CsPb_{1-x}Sn_xCl_3$ systems demonstrate relative instability at 100 K, resulting in phase segregation near Sn- and Pb-derived compositions, as well as compositions approaching the Sn limit. Conversely, the metastability and phase segregation region for $CsPb_{1-x}Sn_xBr_3$ alloys manifest at considerably lower temperatures, in compositions with higher concentrations of Pb.

In the isostructural limits (Figure S7 in Supplementary Materials), it can be observed that the polymorphic patterns with $a^0b^+b^+$ and $a^0b^-b^+$ symmetry have higher critical temperatures in the $0.0 < x < 1.0$ and $0.2 < x < 0.6$ regions for $CsPb_{1-x}Sn_xCl_3$ alloy, while $a^0a^0a^0$ and $a^+a^-a^+$ form more stable solid solutions. The phase-segregation regions demonstrates increased susceptibility to high Pb concentrations, whereas Sn-rich alloys exhibit a reduced response. However, given that $a^-a^+a^-$ is the polymorphic form with the most significant contribution in Pb–rich compositions, the remaining contributions to the APD ensemble are reduced, thereby generating the observed behavior. This phenomenon can be discerned in the results of $\Delta_{mix}F$. In the pure metal compositions, particularly in the composition with Pb, the alloy exhibits increased instability compared to the alloy with excess Sn.

A similar behavior is observed in $CsPb_{1-x}Sn_xBr_3$ alloy, characterized by low critical temperatures and the absence of phase segregation for $a^+a^-a^+$ polymorph. Therefore, in the context of APD statistics, the regions of (meta)instability become more pronounced for $CsPb_{1-x}Sn_xCl_3$, with phase segregation regions at cryogenic temperatures near $x = 0.5$ region, and a smaller miscibility gap with excess Sn. Conversely, for $CsPb_{1-x}Sn_xBr_3$ alloy, the miscibility gap becomes wider due to the contribution of polymorphs in the central region, but at an extremely low critical temperature of 28 K.

3.2. Polymorphic Effects on the Gap Energy

To describe the behavior of gap energy in response to gradual changes in the $CsPb_{1-x}Sn_xCl_3$ and $CsPb_{1-x}Sn_xBr_3$ alloys composition, we analyzed gap energy values considering statistical APD across average values using the GQCA approach. The results obtained through the DFT-1/2+SOC approach are shown in Figure 6, with experimental reports being represented as green filled circles, as well as the isostructural Glazer alloys in Figure S8 in Supplementary Materials.

As expected, the gap energies (E_g) exhibit a decreasing trend with increasing Sn content, a trend driven by the narrow-gap nature of Sn–based MHPs and the reduced electronegativity difference between the halide and the B-site cation. However, as indicated by the shaded regions representing statistical uncertainty, the $CsPb_{1-x}Sn_xCl_3$ system (panel a) displays significant deviations from the expected Vegard-like linearity. This anomalous behavior is particularly pronounced in the $a^0b^-b^+$ and $a^+a^-a^+$ polymorphs, where the high sensitivity of the Cl-lattice to octahedral tilting induces a non-monotonic evolution of the electronic profiles. Such departures from the ideal trend coincide with compositions where in-phase and out-of-phase Glazer rotations coexist. The observed curvature in E_g is concomitant with the non-linear distortion of Cl–B–Cl bond angles, as corroborated by the structural analysis in Figure 2. Consequently, the application of APD analysis is essential to decouple the statistical contributions of diverse polymorphic states at x_k, thereby elucidating the structural origins of the observed gap changes.

Our results, obtained via statistical averaging, show good agreement with experimental values, demonstrating the robustness of the DFT– 1/2+SOC method for calculating the gap energy of MHPs. Furthermore, Table S22 in the Supplementary Materials presents literature values for the pure compounds calculated using HSE/HSE06+SOC. The results obtained through the APD are in excellent agreement with both experimental reports and HSE06+SOC calculations from the literature, further validating the reliability of the proposed protocol. Notably, the DFT– 1/2+SOC protocol employed here is computationally efficient, as its computational cost is comparable to that of the standard DFT-PBE approach.[23]

Downloaded from http://pubs.acs.org/aaemcq/article-pdf/doi/10.1021/acsaem.6c01421/65829129/ae-2026-014215.pdf by KIT BIBLIOTHEK user on 27 July 2026

https://doi.org/10.1021/acsaem.6c01421
ACS Appl. Energy Mater. 2026, 9, 9445−9455

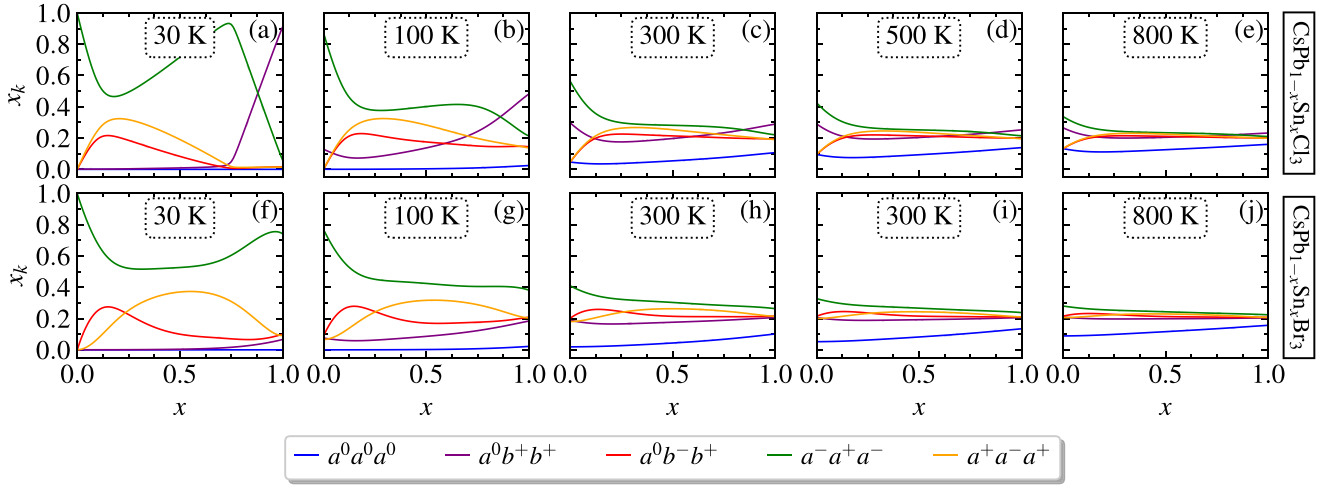

Figure 4. Polymorph probabilities (x_k) as a function of composition by considering the APD statistics for $CsPb_{1-x}Sn_xCl_3$ calculated at (a) 30 K, (b) 100 K, (c) 300 K, (d) 500 K, and (e) 800 K and $CsPb_{1-x}Sn_xBr_3$ calculated at (f) 30 K, (g) 100 K, (h) 300 K, (i) 500 K, and (j) 800 K.

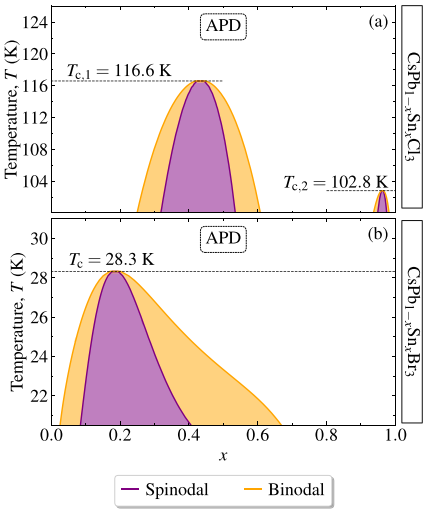

Figure 5. Phase diagrams calculated as a function of composition (x) and temperature (T) by considering all polymorphic degrees (APD) of the (a) $CsPb_{1-x}Sn_xCl_3$ and (b) $CsPb_{1-x}Sn_xBr_3$ alloys. The spinodal regions are depicted in purple, while the metastable ones are shown in orange. In the white region, the solid solution is stable against phase segregation. Dashed lines indicate the critical temperatures (T_c).

The synthesis of $CsPb_{1-x}Sn_xCl_3$ alloy into all the x-compositions interval is very scarce, given that we have kept the experiment references for $x = 0$ and $x = 1$, where one observes deviations of around −9.3 and −1.8%, respectively, from the average calculated over APD model through our DFT-1/2+SOC protocol. However, based on our previous studies[8,10,23,60] for the band gap tuning and impact of the polymorphism throughout $x = 0 \rightarrow 1$ composition interval, our approach contributes to the design of this alloy from a predictive perspective for the band gap tuning.

Additionally, a sharp curvature is also observed when the Pb composition of the alloys decreases. Known as the bowing parameter (b) for the band gap of alloys, it can be calculated using the expression $E_g(x) = (1 - x)\ E_g(CsPbX_3) + x\ E_g(CsSnX_3) + b(x)\ x\ (1 - x)$ (X = Cl or Br). The dependence of b on x is shown in Figure S9 in Supplementary Materials. The non-linear behavior of the parameter b is evident, resulting from both structural variations and changes in the magnitude of the spin-orbit coupling contribution, which is greater in Pb-rich compositions.[41]

3.3. Optical Absorption Coefficient and PCE from the SLME Model Combined with GQCA

The PCE of the $CsPb_{1-x}Sn_xCl_3$ and $CsPb_{1-x}Sn_xBr_3$ alloys was subsequently calculated, with the aim of investigating its potential application in solar cells. The PCE values utilizing the SLME approach with DFT-1/2+SOC gaps are presented in Figure 7. These values were calculated from the mean GQCA ensemble in the APD statistic at 300 K. The curves for $CsPb_{1-x}Sn_xCl_3$ and $CsPb_{1-x}Sn_xBr_3$ reveal that, in general, smaller gaps are related to higher PCE values (see Figure 6). However, the PCE values of the $CsPb_{1-x}Sn_xCl_3$ alloy show a steep curve at the limits of the pure compositions, with $CsPbCl_3$ at 7% and $CsSnCl_3$ at 17%, and a maximum value at $x = 0.75$ (19%). This phenomenon can be attributed to the gap energies of the isostructural limits and the contribution of the polymorphism (x_k) at 300 K (Figure S8). For $CsPb_{1-x}Sn_xCl_3$, the behavior can be associated with the significant increase in E_g observed for the $a^0b^+b^+$ polymorph in Sn-rich compositions. As evidenced by the x_k analyses at 300 K, this polymorph becomes the dominant contribution to the thermodynamic ensemble at high Sn concentrations. Since this structure exhibits considerably larger gap energies, the resulting blue-shift drastically reduces the calculated PCE values, even in Sn-rich compositions where lower gap energies would normally be expected.

In contrast, $CsPb_{1-x}Sn_xBr_3$ exhibits a different behavior. In this alloy, the dominant polymorph at high Sn concentrations does not present the same anomalous increase in E_g observed for the chloride counterpart. On the one hand, the substitution of Pb by Sn reduces E_g, which would tend to increase the PCE. However, Sn-based compounds exhibit intrinsically lower optical absorption than Pb-based compounds, partly due to the smaller number of electrons in the Sn atom, which reduces the absorption strength and consequently the conversion

https://doi.org/10.1021/acsaem.6c01421
ACS Appl. Energy Mater. 2026, 9, 9445−9455

Downloaded from http://pubs.acs.org/aaemcq/article-pdf/doi/10.1021/acsaem.6c01421/65829129/ae-2026-014215.pdf by KIT BIBLIOTHEK user on 27 July 2026

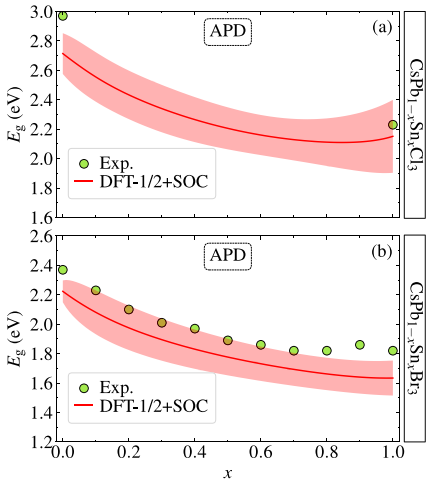

Figure 6. Gap energies (E_g) calculated as a function of composition at room temperature (300 K) by considering all polymorphic degrees (APD) of the (a) $CsPb_{1-x}Sn_xCl_3$ and (b) $CsPb_{1-x}Sn_xBr_3$ alloys. Experimental references, when available, are shown as filled symbols and were taken from references: $CsPbCl_3$,[57] $CsSnCl_3$,[58] and $CsPb_{1-x}Sn_xBr_3$.[59]

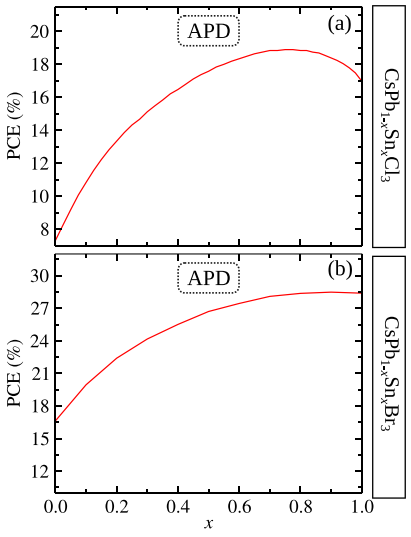

Figure 7. Calculated power conversion efficiency (PCE) for (a) $CsPb_{1-x}Sn_xCl_3$ and (b) $CsPb_{1-x}Sn_xBr_3$ through APD GQCA statistics via the SLME model, considering the alloy thickness as 1 μm and T = 300 K.

efficiency. The competition between band gap narrowing (positive contribution to PCE) and reduced optical absorption (negative contribution) results in the nearly constant PCE profile observed for $CsPb_{1-x}Sn_xBr_3$. Consequently, the PCE exhibits a plateau around its maximum value of approximately 29% in the x = 0.7–1.0 interval.

Interestingly, the highest value of PCE occurs in both cases before the compositions with narrow gap energies (i.e., x = 1.0). To understand this behavior, we correlated the APD gap energies and total absorbance as a function of composition at 300 K, Figure 8. The optical absorption profile of the alloys is

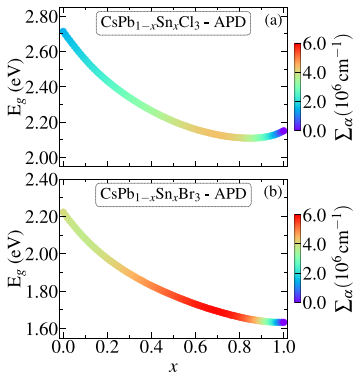

Figure 8. Correlation between the gap energy, composition, and total absorption coefficient ($\sum_\alpha$) calculated for (a) $CsPb_{1-x}Sn_xCl_3$ and (b) $CsPb_{1-x}Sn_xBr_3$ through APD GQCA statistics at 300 K. The color map corresponds to the $\sum_\alpha$ obtained via GQCA for the photon energy range 0.0–4.0 eV.

shown in Figure S10 of the Supplementary Materials. This analysis reveals that the higher PCE of x = 0.7 ($0.5 < x < 0.8$) for $CsPb_{1-x}Sn_xCl_3$ ($CsPb_{1-x}Sn_xBr_3$) arises from a compensatory effect between E_g and $\sum_\alpha$, since the gap energy is only slightly lower toward this region of both halide compositions, while its total absorbance is greater than the pristine $CsSnX_3$ in both cases. However, since pure Sn-based MHP is more prone to oxidation in air than its Pb-based counterpart,[61–63] the use of an alloy could reduce this tendency while increasing the desired long-term stability of photovoltaic devices.[64–66] Considering that the miscibility gaps in this region exhibit low critical temperatures, around T =120 K for $CsPb_{1-x}Sn_xCl_3$ and 28.3 K for $CsPb_{1-x}Sn_xBr_3$, this range of compositions becomes extremely viable for stable devices.

Notably, the SLME quantifies the optoelectronic ceiling imposed by the absorber's band structure and absorption spectrum alone.[34] Contributions from non-radiative recombination (Shockley-Read-Hall, Auger), carrier mobility, interfacial losses and oxidative degradation lie outside its scope.[67] The interplay of these factors ultimately determines the efficiency of a fabricated device.

4. CONCLUSIONS

In summary, first-principles calculations were performed on the polymorphic behavior of $CsPb_{1-x}Sn_xX_3$ (X = Cl, Br) alloys, which were able to highlight the combined impact of composition and polymorphism on structural, electronic, and thermodynamic stability properties. The thermodynamic properties exhibited high sensitivity to specific polymorphic patterns, particularly in $CsPb_{1-x}Sn_xCl_3$, where the smaller ionic radius of Cl relative to Br amplifies structural distortions. In both alloys the role of the polymorphic characteristics is crucial for thermodynamic stabilization process under solar cell operating conditions, i.e., for $T > 0$ K, since the high symmetry configuration such as $a^0a^0a^0$ contributes minimally compared to the other polymorphic configurations. Critical temperatures were found to be approximately 110 K and 28.3 K for Cl- and Br-containing alloys, respectively, thereby broadening the device operating range and reducing the risk of phase-segregation-driven instability. Our model was able to capture the weighted polymorphic

https://doi.org/10.1021/acsaem.6c01421
ACS Appl. Energy Mater. 2026, 9, 9445−9455

Downloaded from http://pubs.acs.org/aaemcg/article-pdf/doi/10.1021/acsaem.6c01421/65829129/ae-2026-014215.pdf by KIT BIBLIOTHEK user on 27 July 2026

contribution on the optoelectronic performance, such that around $x = 0.70$, both compositions exhibit the highest PCE values, e.g., ranging from above 19 to 29%, in particular for $CsPb_{1-x}Sn_xBr_3$ by conferring a notable Pb content reduction and keeping the PCE around 29% for the $x = 0.7–1.0$ interval.

■ ASSOCIATED CONTENT

Data Availability Statement

The data supporting our findings in this study are available within the main text and its supplementary materials. The raw data supporting the conclusions of this article will be made available by the authors upon reasonable request. The WaNos code, workflow information, and additional simulation data are public in our GitHub repository at https://github.com/KIT-Workflows/TMD-Alloy.

Supporting Information

The Supporting Information is available free of charge at https://pubs.acs.org/doi/10.1021/acsaem.6c01421.

Additional results for the geometric and electronic properties (PDF)

■ AUTHOR INFORMATION

Corresponding Authors

Danilo Neves Silveira – *Quantum Chemistry and Thermodynamic Materials, Chemistry Department, Federal University of Paraná, Curitiba 81531-980, Brazil;* Email: daniloneves@ufpr.br

Diego Guedes-Sobrinho – *Quantum Chemistry and Thermodynamic Materials, Chemistry Department, Federal University of Paraná, Curitiba 81531-980, Brazil;* orcid.org/0000-0002-3313-2822; Email: guedessobrinho@ufpr.br

Authors

Luis Octavio de Araujo – *Department of Chemistry, Federal University of Technology of Paraná, Ponta Grossa, PR 84017-220, Brazil*

Marco Antônio Andrade Queiroz – *Quantum Chemistry and Thermodynamic Materials, Chemistry Department, Federal University of Paraná, Curitiba 81531-980, Brazil*

Celso R. C. Rêgo – *Institute of Nanotechnology Hermann-von-Helmholtz-Platz, Karlsruhe Institute of Technology, Karlsruhe 76021, Germany*

Carlos Maciel de O. Bastos – *Physical Institute and International Center for Physics, University of Brasília, Brasília, DF 70919-970, Brazil*

Maurício J. Piotrowski – *Department of Physics, Federal University of Pelotas, P.O. Box 354, Pelotas, RS 96010-900, Brazil*

Alexandre C. Dias – *Physical Institute and International Center for Physics, University of Brasília, Brasília, DF 70919-970, Brazil*

Fernando P. Sabino – *Department of Materials Engineering, São Carlos School of Engineering, University of São Paulo, São Carlos, SP 13563-120, Brazil*

Complete contact information is available at: https://pubs.acs.org/doi/10.1021/acsaem.6c01421

Author Contributions

Diego Guedes-Sobrinho and **Danilo Neves Silveira** conceptualized this research, guided the data analysis/interpretation, and the manuscript writing; **Diego Guedes-Sobrinho**, **Danilo Neves Silveira** and **Luis Octavio de Araujo** performed the calculations and the preliminary formal analysis, as well as the manuscript writing; **Celso R. C. Rêgo** developed the SimStack Wanos; **Maurício J. Piotrowski**, **Marco Antônio Andrade Queiroz**, **Alexandre C. Dias** and **Carlos Maciel de O. Bastos** performed formal analysis and tests on the SimStack platform; **Fernando P. Sabino** contributed to the discussion of the results and revised the manuscript; **Danilo Neves Silveira** and **Diego Guedes-Sobrinho** reviewed earlier drafts to produce the final version of the paper. All authors contributed to additional calculations, writing, data analysis, and manuscript revision.

Funding

The Article Processing Charge for the publication of this research was funded by the Coordenacao de Aperfeicoamento de Pessoal de Nivel Superior (CAPES), Brazil (ROR identifier: 00x0ma614).

Notes

The authors declare no competing financial interest.

■ ACKNOWLEDGMENTS

The authors thank the Ogun Computer at CIMATEC SENAI (Salvador—BA), "Centro Nacional de Processamento de Alto Desempenho em São Paulo"(CENAPAD-SP, UNICAMP/FINEP—MCTI, under projects n.897 and n.570), Lobo Carneiro HPC (NACAD) at the Federal University of Rio de Janeiro (UFRJ, project n.133), and SDumont supercomputer for the support to perform the calculations. The authors gratefully acknowledge the Karlsruhe Institute of Technology (KIT) for the HoreKa supercomputer resources. D.N.S. thanks the Coordination for Improvement of Higher Level Education—CAPES (finance Code 001) for funding. The authors are also thankful for financial support from the National Council for Scientific and Technological Development (CNPq, grant numbers 409792/2024-1, 307345/2021-1, 408144/2022-0, 313081/2017-4, 303206/2025-0, 444431/2024-1, and 305335/2020-0), Federal District Research Support Foundation (FAPDF, grants 00193-00001817/2023-43 and 00193-00002073/2023-84), and the Rio Grande do Sul Research Foundation (FAPERGS, grant number 24/2551-0001551-5). F.P.S. thanks the FAPESP under grant (2025/02193-8) and CNPq (304205/2025-7). W.W. and C.R.C.R. thank the German Federal Ministry of Education and Research (BMBF) for financial support of the project Innovation-Platform MaterialDigital (www.materialdigital.de) through project funding FKZ number 13XP5094A.

■ REFERENCES

(1) Leijtens, T.; Eperon, G. E.; Noel, N. K.; Habisreutinger, S. N.; Petrozza, A.; Snaith, H. J. Stability of Metal Halide Perovskite Solar Cells. *Adv. Energy Mater.* **2015**, *5*, 1500963.

(2) Yang, R.; Yang, D.; Liu, S. F. High-Performance All-Inorganic Cesium Halide Perovskite Solar Cells. *Chem. Rev.* **2026**, *126*, 1408–1469.

https://doi.org/10.1021/acsaem.6c01421
ACS Appl. Energy Mater. 2026, 9, 9445–9455

Downloaded from http://pubs.acs.org/aaemcq/article-pdf/doi/10.1021/acsaem.6c01421/65829129/ae-2026-014215.pdf by KIT BIBLIOTHEK user on 27 July 2026

(3) Park, J.; Kim, J.; Yun, H.-S.; Paik, M. J.; Noh, E.; Mun, H. J.; Kim, M. G.; Shin, T. J.; Seok, S. I. Controlled Growth of Perovskite Layers with Volatile Alkylammonium Chlorides. *Nature* **2023**, *616*, 724–730.
(4) Green, M. A.; Dunlop, E. D.; Yoshita, M.; Kopidakis, N.; Bothe, K.; Siefer, G.; Hao, X. Solar cell efficiency tables (version 62). *Prog. Photovoltaics Res. Appl.* **2023**, *31*, 651–663.
(5) Green, M. A.; Emery, K.; Hishikawa, Y.; Warta, W.; Dunlop, E. D. Solar Cell Efficiency Tables (version 39). *Prog. Photovoltaics Res. Appl.* **2012**, *20*, 12–20.
(6) Juarez-Perez, E. J.; Hawash, Z.; Raga, S. R.; Ono, L. K.; Qi, Y. Thermal Degradation of $CH_3NH_3PbI_3$ Perovskite into NH_3 and CH_3I Gases Observed by Coupled Thermogravimetry–Mass Spectrometry Analysis. *Energy Environ. Sci.* **2016**, *9*, 3406–3410.
(7) Aktas, E.; Rajamanickam, N.; Pascual, J.; Hu, S.; Aldamasy, M. H.; Di Girolamo, D.; Li, W.; Nasti, G.; Martínez-Ferrero, E.; Wakamiya, A., et al.Challenges and Strategies toward Long-Term Stability of Lead-Free Tin-Based Perovskite Solar Cells. *Commun. Mater.* **2022**, *3*, 104.
(8) de Araujo, L. O.; Rêgo, C. R. C.; Wenzel, W.; Sabino, F. P.; Guedes-Sobrinho, D. Impact of the Polymorphism and Relativistic Effects on the Electronic Properties of Inorganic Metal Halide Perovskites. *J. Phys. Chem. C* **2022**, *126*, 2131–2140.
(9) de Araujo, L. O.; Rêgo, C. R.; Wenzel, W.; Piotrowski, M. J.; Dias, A. C.; Guedes-Sobrinho, D. Automated Workflow for Analyzing Thermodynamic Stability in Polymorphic Perovskite Alloys. *NPJ Comput. Mater.* **2024**, *10*, 146.
(10) de Araujo, L. O.; Rêgo, C. R.; Wenzel, W.; Silveira, D. N.; Piotrowski, M. J.; Sabino, F. P.; Pramudya, Y.; Guedes-Sobrinho, D. How Cation Nature Controls the Bandgap and Bulk Rashba Splitting of Halide Perovskites. *J. Comput. Chem.* **2023**, *44*, 1395–1403.
(11) Tsvetkov, D. S.; Mazurin, M. O.; Sereda, V. V.; Ivanov, I. L.; Malyshkin, D. A.; Zuev, A. Y. Formation Thermodynamics, Stability, and Decomposition Pathways of $CsPbX_3$ (X = Cl, Br, I) Photovoltaic Materials. *J. Phys. Chem. C* **2020**, *124*, 4252–4260.
(12) Dehingia, A.; Das, U.; Roy, A. Compositional Engineering in α-$CsPbI_3$ toward the Efficiency and Stability Enhancement of All Inorganic Perovskite Solar Cells. *ACS Appl. Energy Mater.* **2022**, *5*, 12099–12108.
(13) Zhao, X.; Dalpian, G. M.; Wang, Z.; Zunger, A. Polymorphous Nature of Cubic Halide Perovskites. *Phys. Rev. B* **2020**, *101*, 155137.
(14) Zhao, X.-G.; Wang, Z.; Malyi, O. I.; Zunger, A. Effect of Static Local Distortions vs. Dynamic Motions on the Stability and Band Gaps of Cubic Oxide and Halide Perovskites. *Mater. Today* **2021**, *49*, 107–122.
(15) Straus, D. B.; Guo, S.; Abeykoon, A. M.; Cava, R. J. Understanding the Instability of the Halide Perovskite $CsPbI_3$ through Temperature-Dependent Structural Analysis. *Adv. Mater.* **2020**, *32*, 2001069.
(16) Weadock, N. J.; MacKeen, C.; Qin, X.; Waquier, L.; Rakita, Y.; Vigil, J. A.; Karunadasa, H. I.; Blum, V.; Toney, M. F.; Bridges, F. Thermal Contributions to the Local and Long-Range Structural Disorder in $CH_3NH_3PbBr_3$. *PRX Energy* **2023**, *2*, 033004.
(17) Sabino, F. P.; Xiong, J.-X.; Zhang, X.; Dalpian, G. M.; Zunger, A. Alloying Multiple Halide Perovskites on the Same Sublattice in Search of Stability and Target Band Gaps. *Mater. Horiz.* **2025**, *12*, 7389–7401.
(18) Dalpian, G. M.; Zhao, X.; Kazmerski, L.; Zunger, A. Formation and Composition-Dependent Properties of Alloys of Cubic Halide Perovskites. *Chem. Mater.* **2019**, *31*, 2497–2506.
(19) Bekemeier, S.; Caldeira Rêgo, C. R.; Mai, H. L.; Saikia, U.; Waseda, O.; Apel, M.; Arendt, F.; Aschemann, A.; Bayerlein, B.; Courant, R.; Dziwis, G.; Fuchs, F.; Giese, U.; Junghanns, K.; Kamal, M.; Koschmieder, L.; Leineweber, S.; Luger, M.; Lukas, M.; Maas, J.; Mertens, J.; Mieller, B.; Overmeyer, L.; Pirch, N.; Reimann, J.; Schröck, S.; Schulze, P.; Schuster, J.; Seidel, A.; Shchyglo, O.; Sierka, M.; Silze, F.; Stier, S.; Tegeler, M.; Unger, J. F.; Weber, M.; Hickel, T.; Schaarschmidt, J. Advancing Digital Transformation in Material Science: The Role of Workflows Within the MaterialDigital Initiative. *Adv. Eng. Mater.* **2025**, *27*, 2402149.
(20) Schaarschmidt, J.; Yuan, J.; Strunk, T.; Kondov, I.; Huber, S. P.; Pizzi, G.; Kahle, L.; Bolle, F. T.; Castelli, I. E.; Vegge, T.; Hanke, F.; Hickel, T.; Neugebauer, J.; Rêgo, C. R. C.; Wentzel, W. Workflow Engineering in Materials Design within the BATTERY 2030+ Project. *Adv. Energy Mater.* **2021**, *12*, 2102638.
(21) Rêgo, C. R.; Schaarschmidt, J.; Schlöder, T.; Penaloza-Amion, M.; Bag, S.; Neumann, T.; Strunk, T.; Wenzel, W. SimStack: An Intuitive Workflow Framework. *Front. Mater.* **2022**, *9*, 877597.
(22) Grau-Crespo, R.; Hamad, S.; Catlow, C. R. A.; De Leeuw, N. Symmetry-Adapted Configurational Modelling of Fractional Site Occupancy in Solids. *J. Phys.: Condens. Matter* **2007**, *19*, 256201.
(23) Guedes-Sobrinho, D.; Guilhon, I.; Marques, M.; Teles, L. K. Thermodynamic Stability and Structural Insights for $CH_3NH_3Pb_{1-x}Si_xI_3$, $CH_3NH_3Pb_{1-x}Ge_xI_3$, and $CH_3NH_3Pb_{1-x}Sn_xI_3$ Hybrid Perovskite Alloys: A Statistical Approach from First Principles Calculations. *Sci. Rep.* **2019**, *9*, 11061.
(24) Hohenberg, P.; Kohn, W. Inhomogeneous Electron Gas. *Phys. Rev.* **1964**, *136*, B864–B871.
(25) Kohn, W.; Sham, L. J. Self-Consistent Equations Including Exchange and Correlation Effects. *Phys. Rev.* **1965**, *140*, A1133–A1138.
(26) Perdew, J. P.; Burke, K.; Ernzerhof, M. Generalized Gradient Approximation Made Simple. *Phys. Rev. Lett.* **1996**, *77*, 3865–3868.
(27) Blöchl, P. E. Projector Augmented-Wave Method. *Phys. Rev. B* **1994**, *50*, 17953–17979.
(28) Kresse, G.; Hafner, J. Ab Initio Molecular Dynamics for Open-Shell Transition Metals. *Phys. Rev. B* **1993**, *48*, 13115–13118.
(29) Kresse, G.; Furthmüller, J. Efficient Iterative Schemes for Ab Initio Total-Energy Calculations Using a Plane-Wave Basis Set. *Phys. Rev. B* **1996**, *54*, 11169–11186.
(30) Ferreira, L. G.; Marques, M.; Teles, L. K. Slater Half-Occupation Technique Revisited: The LDA-1/2 and GGA-1/2 Approaches for Atomic Ionization Energies and Band Gaps in Semiconductors. *AIP Adv.* **2011**, *1*, 032119.
(31) Ferreira, L. G.; Pelá, R. R.; Teles, L. K.; Marques, M.; Ribeiro Jr., M.; Furthmüller, J. The LDA-1/2 technique: Recent developments. *AIP Conf. Proc.* **2013**, *1566*, 27–28.
(32) Slater, J. C.; Johnson, K. H. Self-Consistent-Field X–α Cluster Method for Polyatomic Molecules and Solids. *Phys. Rev. B* **1972**, *5*, 844–853.
(33) Janak, J. F. Proof that $\frac{\partial E}{\partial n_i} = \varepsilon$ in Density-Functional Theory. *Phys. Rev. B* **1978**, *18*, 7165–7168.
(34) Yu, L.; Zunger, A. Identification of Potential Photovoltaic Absorbers Based on First-Principles Spectroscopic Screening of Materials. *Phys. Rev. Lett.* **2012**, *108*, 068701.
(35) Shockley, W.; Queisser, H. J. Detailed Balance Limit of Efficiency of P-N Junction Solar Cells. *Jpn. J. Appl. Phys.* **1961**, *32*, 510–519.
(36) Barhoumi, M. First-Principles Calculations to Investigate Electronic Band Structure, Optical and Mechanical Properties of New CaFCl Monolayer. *Results Phys.* **2023**, *45*, 106251.
(37) Diery, W. Electronic and Optical Properties of New Pentagonal Janus PtXY (X, Y = S, Se, Te; X ≠ Y) Monolayers: A DFT Study. *Phys. B Condens. Matter* **2023**, *669*, 415308.
(38) Gajdos, M.; Hummer, K.; Kresse, G.; Furthmüller, J.; Bechstedt, F. Linear Optical Properties in the Projector-Augmented Wave Methodology. *Phys. Rev. B* **2006**, *73*, 045112.
(39) Hu, B. Y. Kramers-Kronig in Two Lines. *Am. J. Phys.* **1989**, *57*, 821–821.
(40) Guedes-Sobrinho, D.; Guilhon, I.; Marques, M.; Teles, K. L. Relativistic DFT-1/2 Calculations Combined with a Statistical Approach for Electronic and Optical Properties of Mixed Metal Hybrid Perovskites. *J. Phys. Chem. Lett.* **2019**, *10*, 4245–4251.
(41) Bastos, C. M. d. O.; Dias, A. C.; de Brito, A. C. F.; Barcelos, I. D.; da Rosa, A. L.; Silveira, D. N.; Piotrowski, M. J.; Wenzel, W.; Rêgo, C. R.; Guedes-Sobrinho, D. First-Principles Statistical Investigation of Thermodynamic Behavior with Excitonic Effects in $Mo_{1-x}W_xSe_2$

Downloaded from http://pubs.acs.org/aaemcg/article-pdf/doi/10.1021/acsaem.6c01421/65829129/ae-2026-014215.pdf by KIT BIBLIOTHEK user on 27 July 2026

Alloys through a Data-Driven Workflow Approach. *J. Mater. Chem. A* **2025**, *13*, 39053–39064.
(42) Dias, A. C.; Silveira, J. F.; Qu, F. WanTiBEXOS: A Wannier-Based Tight Binding Code for Electronic Band Structure, Excitonic and Optoelectronic Properties of Solids. *Comput. Phys. Commun.* **2023**, *285*, 108636.
(43) Dias, A. C.; Lima, M. P.; Da Silva, J. L. F. Role of Structural Phases and Octahedra Distortions in the Optoelectronic and Excitonic Properties of $CsGeX_3$ (X = Cl, Br, I) Perovskites. *J. Phys. Chem. C* **2021**, *125*, 19142–19155.
(44) Yang, R. X.; Skelton, J. M.; da Silva, E. L.; Frost, J. M.; Walsh, A. Spontaneous Octahedral Tilting in the Cubic Inorganic Cesium Halide Perovskites $CsSnX_3$ and $CsPbX_3$ (X = F, Cl, Br, I). *J. Phys. Chem. Lett.* **2017**, *8*, 4720–4726.
(45) Glazer, A. M. The Classification of Tilted Octahedra in Perovskites. *Acta Crystallogr., Sect. B: Struct. Crystallogr. Cryst. Chem.* **1972**, *28*, 3384–3392.
(46) de Araujo, L. O.; Rego, C. R.; Wenzel, W.; de Oliveira Bastos, C. M.; Piotrowski, M. J.; Dias, A. C.; Guedes-Sobrinho, D. Thermodynamic Modeling and Electronic Properties of $CsPb_{1-x}Sn_xI_3$ as a Polymorphic Alloy. *J. Alloys Compd.* **2024**, *992*, 174485.
(47) de Araujo, L. O.; Sabino, F. P.; Rêgo, C. R. C.; Guedes-Sobrinho, D. Bulk Rashba Effect Splitting and Suppression in Polymorphs of Metal Iodine Perovskites. *J. Phys. Chem. Lett.* **2021**, *12*, 7245–7251.
(48) Schleife, A.; Eisenacher, M.; Rödl, C.; Fuchs, F.; Furthmüller, J.; Bechstedt, F. Ab initio Description of Heterostructural Alloys: Thermodynamic and Structural Properties of $Mg_xZn_{1-x}O$ and $Cd_xZn_{1-x}O$. *Phys. Rev. B* **2010**, *81*, 245210.
(49) Aidhy, D. S.; Wolverton, C. First-Principles Prediction of Phase Stability and Crystal Structures in Li-Zn and Na-Zn Mixed-Metal Borohydrides. *Phys. Rev. B Condens.* **2011**, *83*, 144111.
(50) Worsdale, M.; Rabis, A.; Fabbri, E.; Schmidt, T. J.; Kramer, D. Conductivity Limits of Extrinsically Doped SnO_2 Supports. *ECS Trans.* **2015**, *69*, 1167.
(51) Kim, Y. Effect of Metal Composition on the Structure of Layer-Structured Cathode Materials for Li-Ion Batteries. *Appl. Phys. A* **2020**, *126*, 556.
(52) Bartel, C. J. Review of Computational Approaches to Predict the Thermodynamic Stability of Inorganic Solids. *J. Mater. Sci. Technol.* **2022**, *57*, 10475–10498.
(53) Rohrer, G. S. *Structure and Bonding in Crystalline Materials*; Cambridge University Press, **2001**.
(54) Barrett, J.; Bird, S. R. A.; Donaldson, J. D.; Silver, J. The Mössbauer Effect in Tin(II) Compounds. Part XI. The Spectra of Cubic Trihalogenostannates(II). *J. Chem. Soc. A* **1971**, 3105–3108.
(55) Denton, A. R.; Ashcroft, N. W. Vegard's Law. *Phys. Rev. A* **1991**, *43*, 3161–3164.
(56) Fu, Y.; Jin, S.; Zhu, X.-Y. Stereochemical Expression of ns2 Electron Pairs in Metal Halide Perovskites. *Nat. Rev. Chem.* **2021**, *5*, 838–852.
(57) Heidrich, K.; Schäfer, W.; Schreiber, M.; Söchtig, J.; Trendel, G.; Treusch, J.; Grandke, T.; Stolz, H. Electronic Structure, Photoemission Spectra, and Vacuum-Ultraviolet Optical Spectra of $CsPbCl_3$ and $CsPbBr_3$. *Phys. Rev. B* **1981**, *24*, 5642.
(58) Voloshinovskii, A. S.; Myagkota, S. V.; Pidzyrailo, N. S.; Tokarivskii, M. V. Luminescence and Structural Transformations of $CsSnCl_3$ Crystals. *J. Appl. Spectrosc.* **1994**, *60*, 226–228.
(59) Schwartz, H. A.; Laurenzen, H.; Marzouk, A.; Runkel, M.; Brinkmann, K. O.; Rogalla, D.; Riedl, T.; Ashhab, S.; Olthof, S. Band-Gap Tuning in All-Inorganic $CsPb_xSn_{1-x}Br_3$ Perovskites. *ACS Appl. Mater. Interfaces* **2021**, *13*, 4203–4210.
(60) Guedes-Sobrinho, D.; Neves Silveira, D.; de Araujo, L. O.; Favotto Dalmedico, J.; Wenzel, W.; Pramudya, Y.; Piotrowski, M. J.; Rêgo, C. R. Revealing the Impact of Organic Spacers and Cavity Cations on Quasi-2D Perovskites via Computational Simulations. *Sci. Rep.* **2023**, *13*, 4446.
(61) Noel, N. K.; Stranks, S. D.; Abate, A.; Wehrenfennig, C.; Guarnera, S.; Haghighirad, A.-A.; Sadhanala, A.; Eperon, G. E.; Pathak, S. K.; Johnston, M. B.; Petrozza, A.; Herz, L. M.; Snaith, H. J. Lead-free Organic-Inorganic Tin Halide Perovskites for Photovoltaic Applications. *Energy Environ. Sci.* **2014**, *7*, 3061–3068.
(62) Zhou, Y.; Zhao, Y. Chemical Stability and Instability of Inorganic Halide Perovskites. *Energy Environ. Sci.* **2019**, *12*, 1495–1511.
(63) Li, H.; Wei, Q.; Ning, Z. Toward High Efficiency Tin Perovskite Solar Cells: a Perspective. *Appl. Phys. Lett.* **2020**, *117*, 060502.
(64) Ogomi, Y.; Morita, A.; Tsukamoto, S.; Saitho, T.; Fujikawa, N.; Shen, Q.; Toyoda, T.; Yoshino, K.; Pandey, S. S.; Ma, T.; Hayase, S. $CH_3NH_3Sn_xPb_{(1-x)}I_3$ Perovskite Solar Cells Covering up to 1060 nm. *J. Phys. Chem. Lett.* **2014**, *5*, 1004–1011.
(65) Liu, T.; Chen, K.; Hu, Q.; Zhu, R.; Gong, Q. Inverted Perovskite Solar Cells: Progresses and Perspectives. *Adv. Energy Mater.* **2016**, *6*, 1600457.
(66) Valadares, F.; Guilhon, I.; Teles, L. K.; Marques, M. Electronic Structure Panorama of Halide Perovskites: Approximated DFT-1/2 Quasiparticle and Relativistic Corrections. *J. Phys. Chem. C* **2020**, *124*, 18390–18400.
(67) Kim, S.; Márquez, J. A.; Unold, T.; Walsh, A. Upper Limit to the Photovoltaic Efficiency of Imperfect Crystals from First Principles. *Energy Environ. Sci.* **2020**, *13*, 1481–1491.

Downloaded from http://pubs.acs.org/aaemcq/article-pdf/doi/10.1021/acsaem.6c01421/65829129/ae-2026-014215.pdf by KIT BIBLIOTHEK user on 27 July 2026

https://doi.org/10.1021/acsaem.6c01421
ACS Appl. Energy Mater. 2026, 9, 9445–9455